Soft Matter

PAPER

View Article Online
View Journal

Cite this: DOI: 10.1039/d6sm00039h

Coating-induced lubrication in granular media: from particle-scale tribology to bulk rheology

F. M. Rocha, *[a] D. Dumont, [a] F. Tapia, [b] A. Gans,[c] V. Bertin, [a] M. Nicolas[a] and O. Pouliquen [a]

Coated granular materials are involved in numerous industrial processes, including powder handling in pharmaceuticals, additive manufacturing, cement production, and food processing, where surface treatments control flowability, prevent agglomeration, and improve product consistency. Despite their widespread use, the influence of coatings on the collective behavior of granular materials remains poorly understood. While dry granular flows are well described by the $\mu(I)$ rheology for frictional, noncohesive particles, many real-world systems involve additional interparticle interactions that fall outside this framework. Here, we investigate how polymer coatings on silica grains modify dry granular rheology by introducing non-Coulombic frictional behavior at the particle scale. Pressure-imposed rheological experiments reveal that coatings activate a low-friction regime in which the bulk friction coefficient and packing fraction approach values typical of frictionless grains. The transition from this lubricated state to a conventional frictional regime depends on both normal stress and shear rate, indicating stress- and velocity-dependent contact mechanics. Tribological measurements show that interparticle friction decreases with coating thickness and sliding velocity, but increases with normal load. Building on these findings, we develop a mean-field rheological model that extends the classical $\mu(I)$ framework to include coating-dependent, non-Coulombic friction. Discrete Element Method simulations incorporating the measured friction law capture the key qualitative features observed experimentally. These results demonstrate that controlled surface coatings provide a powerful route to engineer granular rheology and enhance flowability across various industrial applications.

Received 13th January 2026,
Accepted 3rd April 2026

DOI: 10.1039/d6sm00039h

rsc.li/soft-matter-journal

1 Introduction

Granular materials play a major role in natural contexts.[1] Understanding how grains interact and behave collectively is crucial to modelling large-scale hazardous flows, such as landslides, debris flows, and snow avalanches. Powders and grains are also ubiquitous in industrial processes, including those in the pharmaceutical, food, and construction sectors. Every day, millions of tons of granular materials are handled, and issues such as clogging, segregation, and intermittent flow can cause major operational disruptions, waste, and economic losses.[2,3] To mitigate such problems, a common strategy is to coat particles with additives that improve their flowability, and extensive empirical knowledge has been accumulated about these processes.[4] However, a general framework that quantitatively explains how coatings modify granular flow behavior remains elusive. Here, we present the first combined experimental, theoretical, and numerical investigation of lubricated granular materials—silica beads coated with a polymeric layer (Fig. 1)—that reveals the microscopic origin of their macroscopic flow properties.

For dry non-coated granular systems, significant progress has been made over the past decades in describing their rheology through the development of the $\mu(I)$ framework. Those materials are composed of rigid grains interacting primarily through frictional contacts. In such systems, the absence of an intrinsic force scale means that the rheology, the material's response to shear under confining pressure, is governed by a single dimensionless parameter, the inertial number I.[5,6] The leading-order rheology of dry granular materials is thus described by two constitutive relationships, linking the bulk friction coefficient μ and the volume fraction ϕ to I. While a complete description of dry granular rheology is still an active area of research, the $\mu(I)$ framework[5,7] and its extensions[8–11] have successfully captured key phenomena in dry systems.

However, when particles are coated with additives—or more generally, when interparticle interactions extend beyond simple Coulombic friction, involving effects such as adhesion,[12,13]

[a] Aix Marseille University, CNRS, IUSTI, 13453 Marseille, France. E-mail: francisco.rocha@cnrs.fr
[b] Institute of Urban and Industrial Water Management, Technische Universität Dresden, 01062 Dresden, Germany
[c] Université de Lorraine, CNRS, LEMTA, Vandoeuvre-lès-nancy, France

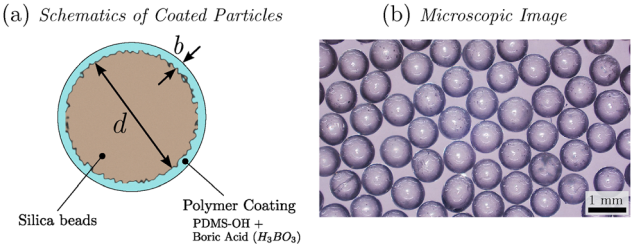

Fig. 1 (a) Schematics of the coated particles (not to scale) and (b) a microscope image of a d = 0.8 mm particle coated with a polymeric layer thickness of b = 35 nm.

elasticity,[14] or electrostaticity[15]—granular systems fall outside the scope of classical $\mu(I)$ rheology. Despite their importance in natural and industrial settings, the role of these microscopic interactions in determining bulk flow behavior remains poorly understood. Establishing a quantitative link between complex microscopic interparticle properties and macroscopic granular rheology, therefore, represents a central open challenge.

In contrast, this connection has been recently explored in the rheology of suspensions, where particles are immersed in a liquid. In these systems, significant efforts have been devoted to tailoring interparticle forces to achieve specific macroscopic flow behaviors. For example, studies have manipulated particle roughness to activate nanoscale frictional modes,[16,17] or have controlled hydrogen bonding between grains.[18,19] Others have introduced surface charges *via* CuAAC click chemistry,[20] or have adjusted the electric double layer by adding salt to the fluid.[21,22] By modulating attraction, repulsion, or friction between particles, it has been possible to successfully tune phenomena such as the onset of shear thickening or shear thinning in suspensions.

While precise control over particle interactions has been achieved in suspensions, this approach remains far less explored in dry granular materials. In the absence of a fluid medium, interactions are inherently more difficult to manipulate, and the rheology of dry granular systems with complex cohesive[12,13] or non-Coulombic interactions[23–25] is still poorly understood.

In this work, we investigate how the addition of a thin polymer coating on silica particles dramatically alters the rheology of granular materials. Polymer-coated silica beads were first introduced by Gans *et al.*[26] as a model system for controlling interparticle adhesion. These sticky particles have since been used in several studies to explore how cohesion influences flow dynamics.[27–30] Here, we demonstrate that the coating not only introduces adhesion but also profoundly affects frictional interactions between grains by inducing lubrication effects, thereby changing the rheology. These findings may have significant implications for industrial processes that use coatings to enhance the flowability of granular materials.[4]

This paper is organized as follows. We first describe the process used to create the coating and characterize the particles. Then, pressure-imposed rheological experiments are conducted to reveal that the coating activates a low-friction state, reducing the bulk friction coefficient to values approaching those of frictionless particles.[25,31,32] We proceed by performing a four-ball tribology test to measure the interparticle friction law for the coated particles and demonstrate that the bulk rheological transition is due to a lubrication mechanism at the grain scale. To understand the link between particle-scale frictional properties and bulk rheological behavior, we develop a mean field model that integrates the coating's influence into an effective interparticle friction coefficient, thereby extending the $\mu(I)$ rheology. The experiments and the model are then compared with Discrete Element Method (DEM) simulations, where the experimentally measured interparticle friction law is embedded into the contact model. The paper concludes with a discussion and final remarks.

2 The coated granular material

The material used in this study consists of spherical glass beads (Decobeads, Sigmund Lindner) with diameters d = [0.8–10.0] mm. The particles are coated with a thin layer of polyborosiloxane (PBS), which is a mixture of –OH terminated polydimethylsiloxane (PDMS, 3 M) cross-linked with boric acid (H_3BO_3, 3 M). The coating thickness, b, typically ranges from 10 to 1000 nm. A schematic representation of the particles and a picture are shown in Fig. 1. By controlling the total mass of grains, m_g, the total mass of PBS, m_p, and assuming a homogeneous distribution of the PBS on the glass particles, the average coating thickness can be computed as follows:

$$b = \frac{d}{2}\left[\left(1+\frac{m_p\rho_g}{m_g\rho_p}\right)^{1/3}-1\right], \quad (1)$$

where $\rho_g = 2500\ \mathrm{kg\ m^{-3}}$ and $\rho_p = 970\ \mathrm{kg\ m^{-3}}$ are the densities of the glass particles and the PDMS, respectively. Particles are coated following the experimental protocol introduced by Gans *et al.* (2020).[26] First, a mass of boric acid equal to 0.14 the mass of PDMS is dissolved in purified water heated at 60 °C, then mixed with the particles and the PDMS. The mixture is thoroughly stirred with a heating mixer at 110 °C for 90 minutes. As the water slowly evaporates, the polymer cross-links with the silica particles, creating a roughly homogeneous coating thickness. The resulting coated granular material is insensitive to temperature and humidity, and because the polymer layer is grafted to the silica particle, no drainage of the coating is observed over several months, ensuring long-term stability. With this coating method, the interparticle interaction remains pairwise for all b.

This material was initially designed as a model cohesive granular medium, where the force required to detach two individual particles, F_c, is a function of the average coating thickness b.[26] It has since been used to investigate the role of cohesion in several configurations, including granular collapse,[27,28] silo discharge,[29] and rotating drums.[30] In all these applications, cohesion was important, as F_c was not negligible compared to the typical stress level. In other words, the

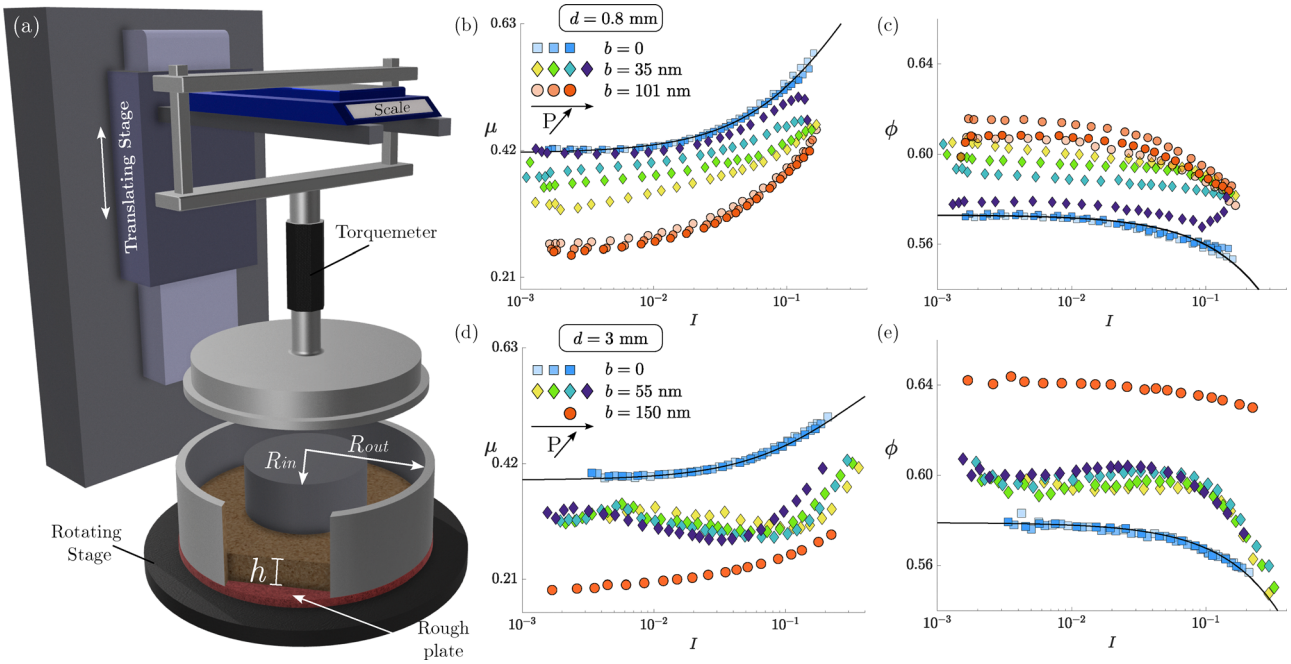

Fig. 2 (a) Experimental set-up of the pressure-imposed rheometer. (b) Bulk friction coefficient μ and (c) solid volume fraction ϕ as a function of the inertial number I for a material composed of glass beads of size d = 0.8 mm, three different coating thickness b, and subjected to constant pressures P = 1100 (♦), 1300 (♦), 1500 (♦), and 1600 (♦) Pa. (d) $\mu(I)$ and (e) $\phi(I)$ for d = 3.0 mm, different coating thickness, with imposed pressures P = 1600 (♦), 2100 (♦), 2600 (♦), and 4100 (♦) Pa. Markers represent experimental data, whilst solid lines are constitutive relationships fitted using eqn (2) and (3) with μ_c = 0.39, μ_d = 0.70, I_0 = 0.35, ϕ_c = 0.579, and ϕ_m = 0.465 for d = 3.0 mm and μ_c = 416, μ_d = 0.95, I_0 = 0.38, ϕ_c = 0.573, and ϕ_m = 0.44 for d = 0.8 mm.

cohesion number defined as $C = F_c/Pd^2$, where P is the typical confining pressure and d the particle size, was greater than 1.

In this study, we focus on the effect of the polymer coating on the frictional properties of the material, rather than adhesion. By using coarse particles, we explore a regime where the characteristic external normal force is at least three orders of magnitude greater than the interparticle adhesion, resulting in a typical cohesion number $C \sim 10^{-3}$. Under these conditions, interparticle adhesion becomes negligible, allowing us to isolate and investigate the effect of the coating on interparticle friction. We begin in the next section by examining the bulk rheology of the coated particles.

3 Pressure-imposed rheology

A schematic of the pressure-imposed rheometer used to access the rheology of the coated particles is shown in Fig. 2(a). The grains are confined within an annular shear cell of inner and outer radii, R_{in} = 4.4 cm and R_{out} = 9.0 cm, respectively. To guarantee the closest to no-slip boundary conditions, the top and bottom plates of the cell are roughened by glueing 3D-printed plates with an irregular roughness typically 3 mm thick. The top plate of the cell is connected to a torquemeter, which gives access to the average shear stress applied by the material on the plate, $\tau = \Gamma/(\pi\bar{r}(R_{out}^2 - R_{in}^2))$, where Γ is the measured torque and $\bar{r} = (R_{out} + R_{in})/2$ is the mean radial position. The whole axis is supported by a scale connected to a translating stage, which adjusts the top position to ensure a constant pressure P throughout the experiments. A position sensor is placed at the top plate of the cell, which measures the gap between the top and bottom plates, h. The base of the cell rotates with a constant angular velocity ω, which determines the shear rate through the granular layer, $\dot{\gamma} = \omega\bar{r}/h$. The volume fraction at each time can be computed as $\phi = (m_g/\rho_g)/V_{total}$, where m_g is the total mass of grains, ρ_g = 2500 kg m^{-3} is the intrinsic density of the glass particles, and $V_{total} = \pi(R_{out}^2 - R_{in}^2)h$ is the total volume within the cell.

Each experimental run is performed at a constant imposed pressure P. The stresses and volumetric changes are monitored continuously to ensure that the system reaches a steady-state regime. For each applied pressure, experiments are performed for different speeds to create an increasing sweep in inertial number $I = \dot{\gamma}d\Big/\sqrt{P/\rho_g}$. For each value of I, the bulk friction coefficient $\mu = \tau/P$ and the solid volume fraction ϕ are measured to determine the constitutive relationships $\mu(I)$, $\phi(I)$ of the granular medium. Experiments are performed with two grain diameters d = 0.8 and 3.0 mm, different coating thickness b, and different imposed pressures P. The constitutive laws μ and ϕ are plotted in Fig. 2(b)–(e).

In the absence of coating, *i.e.* b = 0, the constitutive laws collapse onto single master curves $\mu(I)$, $\phi(I)$ for dry granular materials, whose expressions are well captured by[5,33]

$$\mu(I, \mu_p) = \mu_c(\mu_p) + \frac{\mu_d(\mu_p) - \mu_c(\mu_p)}{1 + I_0(\mu_p)/I}, \qquad (2)$$

$$\phi(I, \mu_p) = \phi_c(\mu_p) + (\phi_m(\mu_p) - \phi_c(\mu_p))I, \quad (3)$$

where the material parameters μ_c, μ_d, I_0, ϕ_c, and ϕ_m depend on the interparticle friction coefficient μ_p.[25,32,34] The solid lines represent the best fits to the data for non-coated particles [blue squares in Fig. 2(b)–(e)].

The behavior changes dramatically when the particles are coated with the polymer layer. For thick polymer layers (b = 101 nm), the bulk friction coefficient of the material drastically decreases, with its quasi-static value (at vanishing I) reduced by a factor 2 (circles in Fig. 2b). Conversely, the solids volume fraction increases, with a quasi-static assembly that is more than 5% denser than the uncoated case (circles in Fig. 2c). For this level of coating, both the bulk friction and the volume fraction do not depend strongly on the applied pressure. The curves for different values of P roughly collapse onto a single curve, just like for the uncoated grains.

When the coating thickness is reduced to b = 35 nm, the constitutive laws no longer collapse onto single curves. Instead, both the bulk friction coefficient and the solids volume fraction become explicitly dependent on the applied pressure (diamonds in Fig. 2b and c). At low pressures (yellow markers), the system exhibits a behaviour similar to the highly-coated beads, characterized by a lower friction coefficient and higher volume fractions. However, under higher imposed pressures, the medium becomes more resistant and looser, *i.e.* the bulk friction μ increases while ϕ globally decreases. As the pressure is further increased, the constitutive laws converge towards the classic $\mu(I)$, $\phi(I)$ relationships observed for uncoated grains (dark blue diamonds in Fig. 2b and c).

The rheology of the coated granular material is also dependent on the shear rate $\dot{\gamma}$. Examining the flow curves for d = 0.8 mm and b = 35 nm in Fig. 2(b) and (c), we observe that, as the inertial number increases, the data systematically deviate from the uncoated curves (blue squares) to approach those of the highly-coated ones (red circles). This suggests that the shear rate plays an opposite role to the pressure. While increasing pressure makes the material more frictional and dilute, increasing the shear rate reduces the resistance and creates denser packing.

The influence of the shear rate on the rheology becomes even more pronounced for a material composed of larger grains. In Fig. 2(d) and (e), we present the constitutive relationships measured for d = 3.0 mm and three different coatings, b = 0, 55, and 150 nm. For both the uncoated (b = 0 nm, blue squares) and the highly coated (b = 150 nm, orange circles) cases, the behavior is the same as for smaller grains d = 0.8 mm. However, for the intermediate coating thickness (b = 55 nm), the flow curves at constant pressures exhibit non-monotonic behaviour. The quasi-static plateau (low I) connects to the inertial regime (high I) through a shear-weakening branch, where the friction coefficient μ decreases and the volume fraction ϕ increases with the inertial number. Since shear-weakening rheologies are intrinsically unstable, they are challenging to access experimentally due to the spontaneous development of localization.[35] To obtain the non-monotonic flow curves presented here, experiments were conducted using very thin granular layers ($h \simeq 6$–$8d$), which stabilize the emergence of shear bands and enable access to the steady-state intrinsic rheology.[36] Interestingly, a similar shear-weakening regime was previously observed in emulsions of hydrogel particles, where the non-monotonic flow behaviour was associated with a non-Coulombic, velocity-dependent interparticle friction coefficient.[37]

To summarize the rheological measurements, our results reveal four key effects of the polymer coating on the macroscopic behaviour of the granular material. (i) The coating reduces the bulk friction coefficient and enables the material to reach denser packings. The flow curves obtained for thick polymer layers closely resemble those predicted by DEM simulation for frictionless particles.[25,32] In these simulations, the quasi-static bulk friction coefficient and volume fraction are $\mu_c(\mu_p = 0) \simeq 0.15$ and $\phi_c(\mu_p = 0) \simeq 0.64$. These values are close to our experimental results for thick layers of polymer, *e.g.* $\mu_c(b = 150\ \text{nm}) = 0.18$ and $\phi_c(b = 150\ \text{nm}) = 0.64$, suggesting that our highly-coated particles approach frictionless asymptotic values. (ii) For intermediate coating thickness, the $\mu(I)$ curves begin to be explicitly dependent on the applied normal stress. The system transitions from a frictionless regime to a more resistant state as the pressure increases. (iii) The shear rate plays a role opposite to that of pressure, in which increasing the shear rate makes the medium less resistant and denser. (iv) The particle size also influences the rheology, amplifying the effect of the shear rate to the point where flow curves become non-monotonic, while reducing the influence of the normal stress.

Our experimental results suggest that the polymer coating induces a transition from a frictional to a frictionless state, governed by the imposed pressure, shear rate, and particle size. To elucidate the microscopic origin of this transition, we present in the next section measurements of interparticle friction properties.

4 Characterizing interparticle friction

4.1 The four ball tribometer

To measure the friction coefficient between two individual grains, we use a classical four-ball tribology test. In this setup, a single particle is rotated on top of three fixed particles arranged in a pyramidal disposition, as shown in Fig. 3(a). The three bottom particles are confined and immobilized by a soft wall, while the top sphere is glued to a rheometer head. The rheometer imposes a constant rotation speed Ω and a normal force N, while measuring the resulting torque $\mathcal{T}$ generated by the sliding of the top ball against the three bottom particles. From a force balance at the contacts, we infer the tangential and normal forces at the contact, $F_t = 4\mathcal{T}\cos(\pi/6)/(3d)$ and $F_n = N/(3\cos(\pi/6))$, respectively. The interparticle friction coefficient is then calculated as $\mu_p = F_t/F_n$. Since the particles are not individually coated but coated in batches of 1 kg, heterogeneities in coating thickness exist from one particle to another within the same batch. To account for this variability, we

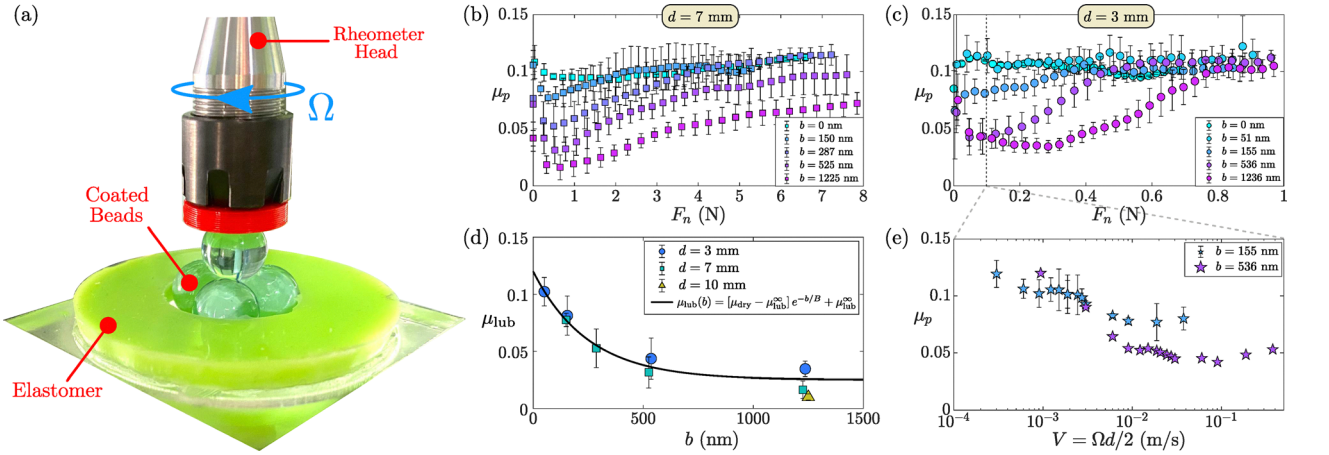

Fig. 3 (a) Experimental set-up used to perform the four-ball tribology test to measure the interparticle friction coefficient. The top sphere is glued to a rheometer head to allow precise control and monitoring of the normal and tangential forces, F_t and F_n, respectively, as well as the sliding velocity. Effective friction coefficient $\mu_p = F_t/F_n$ as a function of the normal force for (b) d = 7.0 mm and (c) d = 3.0 mm, a fixed sliding velocity V = 1.0 mm s^{-1}, and different coating thickness. (d) The value of the lower friction plateau μ_{lub} as a function of the coating thickness for different particle diameters d = 3.0, 7.0, 10.0 mm. (e) Interparticle friction coefficient as a function of the sliding velocity for d = 3.0 mm and fixed normal force F_n = 0.1 N.

systematically averaged our tribology measurements over at least 3 different sets of 4 particles for a given average coating thickness b. With this experimental setup, we were limited to a particle size range of 3–10 mm. For the smallest beads, the torque signal remained below the reliable measurement range of the rheometer, while for larger particles, our protocol failed to produce a sufficiently homogeneous coating.

Fig. 3(b) shows the measured interparticle friction coefficient μ_p for particles with a diameter d = 7 mm at a fixed value of the sliding velocity $V = \Omega d/2$ = 1 mm s^{-1}. For different coating thickness b (indicated by different colors), we plot the variation of the friction coefficient as a function of the normal force F_n at the contact. For uncoated beads (b = 0), the friction remains constant independent of F_n, with a value of μ_{dry} = 0.11 ± 0.01, corresponding to the dry glass-glass friction coefficient.[38] In the presence of the coating, however, the friction coefficient is no longer constant. At low normal forces, it starts at a value $\mu_{lub}(b)$ lower than the glass-glass friction coefficient, indicating a lubrication effect induced by the coating. As the normal force increases, μ_p increases and ultimately approaches the glass–glass friction value at high normal forces. A similar trend is observed for smaller beads with a diameter of d = 3 mm, as shown in Fig. 3(c). While the reduction in friction at low forces appears comparable to that for d = 7 mm, the typical force at which the transition from low to high friction occurs is one order of magnitude lower for d = 3 mm.

To quantify the reduction of friction, or lubrication effect, Fig. 3(d) shows the minimum friction coefficient at low force, *i.e.* lubricated friction, μ_{lub} as a function of the coating thickness b. The data show that μ_{lub} clearly decreases with increasing b, and this trend is accurately described by an exponential fit (solid lines in Fig. 3(d)), as

$$\mu_{lub}(\tilde{b}) = (\mu_{dry} - \mu_{lub}^{\infty})e^{-\tilde{b}} + \mu_{lub}^{\infty}, \quad \text{with } \tilde{b} = b/B, \qquad (4)$$

where μ_{dry} = 0.11 is the non-coated particle friction, μ_{lub}^{∞} = 0.02 is the asymptotic friction value for the thick coating layer, and B = 287 nm is a characteristic length scale over which μ_{lub} decreases from μ_{dry} to μ_{lub}^{∞}. Interestingly, the minimum friction coefficient follows the same exponential law for all three particle sizes, as shown by the different markers in Fig. 3(d). We stress that previous studies have likewise reported that the coating-induced interparticle adhesive force saturates with coating thickness following an exponential law with a characteristic length of the same order of magnitude.[26] We suspect that the particle roughness is the underlying microscopic length governing the saturation of both friction and adhesive interactions with coating thickness.

The interparticle friction coefficient is also affected by the contact sliding velocity V. As shown in Fig. 3(e), the sliding velocity V plays a role opposite to that of pressure, *i.e.* for a given coating thickness b and applied normal force F_n, an increase of the relative velocity between the particles reduces the friction coefficient, driving the transition from a high- to low-frictional contact. Targeting a mean-field model describing the bulk rheology, we will first develop an analytical description of the lubrication transition observed at the interparticle contact.

5 An analytical description of the lubrication transition

The observation that the friction coefficient depends on both the normal force and the sliding velocity is reminiscent of contact tribology in the presence of a liquid lubricant. A lubrication transition is traditionally described by a Stribeck curve, which characterizes how the friction coefficient varies as a function of a dimensionless Hersey number, He = $\eta\lambda V/F_n$, where η is the viscosity of the lubricant, V is the sliding velocity,

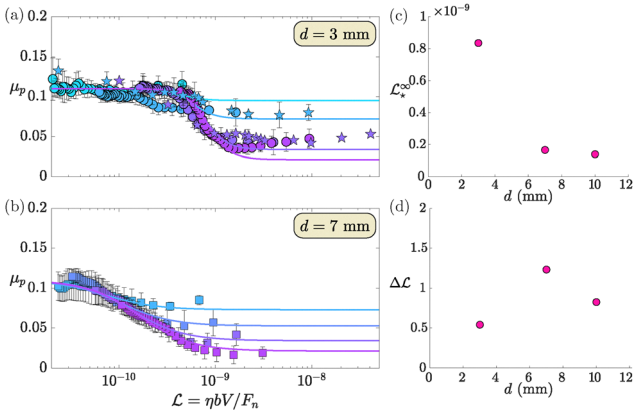

Fig. 4 Interparticle friction law as a function of the lubrication number $\mathcal{L}$ for (a) d = 3 and (b) 7 mm, different applied normal forces F_n, sliding velocities V, and coating thickness b (coded with the same colour code as in Fig. 3). Star symbols represent data for d = 3.0 mm and F_n = 0.1 N for which the sliding velocity was changed while keeping the normal force constant. (c) The lubrication number at the transition, $\mathcal{L}_\star^\infty$, and (d) the width of the transition, $\Delta\mathcal{L}$, for different particles sizes d = 3, 7 and 10 mm.

F_n the normal load at the contact, and λ a characteristic length scale, often associated with curvature radius or Hertz-indentation scale depending on the study.[39–41] A classical Stribeck curve shows that the friction coefficient starts at a high value (corresponding to the solid friction coefficient) when He is small, and decreases to a minimum corresponding to a lubricated state. Then, it increases again at high He values, corresponding to the hydrodynamic regime, where viscous dissipation becomes predominant. While it is known that this description is not fully accurate, and that the Hersey number alone is insufficient to capture transitions between regimes,[42] we nevertheless attempt an analysis of our data within this framework.

Although our coating is not a simple Newtonian fluid but rather a reticulated polymer, an elasto-visco-plastic medium, we introduce a lubrication number $\mathcal{L}$ inspired by the Hersey number and defined as

$$\mathcal{L} = \frac{\eta V b}{F_n}, \tag{5}$$

which uses the coating thickness as the characteristic length scale $\lambda = b$. Here η = 0.750 Pa s is the viscosity of the non-reticulated PDMS used in the coating (kept constant in this study). When the interparticle friction coefficient μ_p, obtained for different coating thicknesses, sliding velocities, and normal loads, is plotted as a function of $\mathcal{L}$, a remarkable collapse of the data is observed at small $\mathcal{L}$, while each data set tends to a plateau value at large $\mathcal{L}$, which is b-dependent. This behavior holds for the two particle sizes investigated (see Fig. 4(a) and (b)). When plotted in semi-log, the curves $\mu_p(\mathcal{L})$ have a step-like form, which can be characterized by a typical transition value $\mathcal{L}_\star$ and a typical width $\Delta\mathcal{L}$, where $\Delta\mathcal{L}$ is the width of the transition in terms of $\log\mathcal{L}$. To attempt an analytical description of this trend, we fit the data with a hyperbolic tangent as an interpolating function, as

$$\mu_p(\mathcal{L},\tilde{b}) = \frac{\mu_{dry}+\mu_{lub}(\tilde{b})}{2} - \frac{\mu_{dry}-\mu_{lub}(\tilde{b})}{2}\left[\tanh\left\{\frac{\log[\mathcal{L}/\mathcal{L}_\star]}{\Delta\mathcal{L}}\right\}\right], \tag{6}$$

where $\mu_{lub}(\tilde{b})$ is the high-$\mathcal{L}$ plateau value, which corresponds to the minimal friction at small force characterized by (4) (see Fig. 3(d)).

The parameters $\mathcal{L}_\star$ and $\Delta\mathcal{L}$ may depend on both b and d. We now analyze those dependencies to identify the key parameters at play. First, we experimentally observe that the b-dependence of $\Delta\mathcal{L}$ is very weak, so that we choose to neglect it for the sake of simplicity. Then, since the curves for different coatings collapse onto a master curve at small $\mathcal{L}$, we utilize this observation to prescribe the functional form of $\mathcal{L}_\star$. We use the following argument: we impose that the value of the interparticle friction at the transition point $\mu_p\left(\mathcal{L}_\star(\tilde{b}),\tilde{b}\right)$ belongs to an underlying master curve $\mu_p\left(\mathcal{L}_\star(\tilde{b}),\infty\right)$, for infinite coating thickness. This condition yields an equation for $\mathcal{L}_\star(\tilde{b})$ that can be solved to get

$$\mathcal{L}_\star = \mathcal{L}_\star^\infty \exp\left\{\Delta\mathcal{L}\,\mathrm{artanh}\left[\frac{\mu_{lub}^\infty-\mu_{lub}(\tilde{b})}{\mu_{dry}-\mu_{lub}^\infty}\right]\right\}. \tag{7}$$

We can then substitute (7) into (6) to obtain the following interparticle friction law

$$\mu_p\left(\frac{\mathcal{L}}{\mathcal{L}_\star^\infty},\tilde{b}\right) = \frac{\mu_{dry}+\mu_{lub}(\tilde{b})}{2} - \frac{\mu_{dry}-\mu_{lub}(\tilde{b})}{2} \times \left[\frac{\tanh\left(\frac{\log(\mathcal{L}/\mathcal{L}_\star^\infty)}{\Delta\mathcal{L}}\right)+\frac{\mu_{lub}(\tilde{b})-\mu_{lub}^\infty}{\mu_{dry}-\mu_{lub}^\infty}}{1+\tanh\left(\frac{\log(\mathcal{L}/\mathcal{L}_\star^\infty)}{\Delta\mathcal{L}}\right)\left(\frac{\mu_{lub}(\tilde{b})-\mu_{lub}^\infty}{\mu_{dry}-\mu_{lub}^\infty}\right)}\right]. \tag{8}$$

The advantage of this substitution is that the b-dependencies are explicit while the two remaining parameters $\mathcal{L}_\star^\infty$ and $\Delta\mathcal{L}$ are functions of d only.

In Fig. 4(a) and (b), the continuous lines represent the best fits given by (8), for particle sizes d = 3 mm and d = 7 mm, where $\mathcal{L}_\star^\infty$ and $\Delta\mathcal{L}$ are adjusted for the entire data set, while $\mu_{lub}(\tilde{b})$, μ_{lub}^∞ and μ_{dry} are fixed. Fig. 4(c) and (d) show how these parameters depend on the particle sizes d. The typical value of the lubrication number at the transition, $\mathcal{L}_\star^\infty$, dramatically increases with decreasing d, while the width of the transition, $\Delta\mathcal{L}$, remains approximately constant.

It is important to note that, although our approach follows the classical Stribeck framework, our results qualitatively differ from traditional Stribeck curves. Specifically, the hydrodynamic regime, where friction typically increases with He at high He, is not observed. Instead, all the data converge to a constant minimum plateau, $\mu_p = \mu_{lub}(\tilde{b})$. This discrepancy may be

attributed to the rheological nature of the PBS coating, which could significantly alter the classic Stribeck behavior.

6 Link between tribology and rheology: a mean field model

The observation of a lubrication transition at the interparticle contact, which depends on both the normal force and the sliding velocity, provides a qualitative explanation for the bulk rheological measurements presented in the previous section. Specifically, the dependence of interparticle friction on the normal force may account for the pressure dependence observed in the rheology, while the influence of sliding velocity may explain the effect of the inertial number on the bulk behavior. However, a major difference arises in the influence of the coating thickness b. While a dramatic effect on the rheology was observed for coating thicknesses less than b = 100 nm, the lubrication transition identified at the particle scale requires much thicker coatings to be effective, typically $b > 200$ nm to start observing an effect. One possible explanation might lie in the heterogeneities of the coating in the granular material or collective effects in the granular assembly that amplify lubrication at smaller thicknesses.

However, keeping in mind this mismatch, which precludes the development of a quantitative model, we derive a simple mean-field approach inspired by previous works[25,43] to better understand how lubrication at the particle scale influences the bulk rheology. The procedure assumes that the rheology is still governed by the Coulombic constitutive laws given by eqn (2) and (3), where we introduce an estimate of the effective interparticle friction μ_p from the phenomenological tribology law derived in the previous section (eqn (8)).

We consider a uniform shear flow at a given confining pressure P and shear rate $\dot{\gamma}$. The order of magnitude of the interparticle sliding velocity is assumed to be given by $V \approx \dot{\gamma} d$, and the order of magnitude of the interparticle normal force is prescribed by the confining pressure: $F_n \approx Pd^2$. Consequently, an estimate of the effective lubrication number (defined in (5)) is $\bar{\mathcal{L}} = \eta b \dot{\gamma} d/(Pd^2)$ which can be rewritten as:

$$\frac{\bar{\mathcal{L}}}{\mathcal{L}_\star^\infty} = I\sqrt{\frac{P_\star}{P}}, \tag{9}$$

where

$$P_\star = \frac{(\eta b)^2}{\rho_g d^4 \mathcal{L}_\star^{\infty 2}} \tag{10}$$

is a characteristic pressure scale that controls the lubrication transition.

With an estimate of the lubrication number, we can infer an averaged interparticle friction coefficient $\bar{\mu}_p\left(\bar{\mathcal{L}}\Big/\mathcal{L}_\star^\infty, \tilde{b}\right)$ from the tribology law (8). Once $\bar{\mu}_p$ is computed, the parameters $\mu_c(\bar{\mu}_p)$, $\mu_d(\bar{\mu}_p)$, $I_0(\bar{\mu}_p)$, $\phi_c(\bar{\mu}_p)$, and $\phi_m(\bar{\mu}_p)$ can be determined (see for instance Appendix A of ref. 25) and substituted in the coulombic constitutive laws eqn (2) and (3) to get a bulk friction law and a solid volume fraction law:

$$\mu = \mu\left(I, \bar{\mu}_p\left(I\sqrt{\frac{P_\star}{P}}, \tilde{b}\right)\right), \tag{11}$$

$$\phi = \phi\left(I, \bar{\mu}_p\left(I\sqrt{\frac{P_\star}{P}}, \tilde{b}\right)\right). \tag{12}$$

From this simple mean field approach, several observations can be made. First, it shows that the bulk rheology is a function of three dimensionless numbers: the inertial number I, the dimensionless pressure $P/P_\star$, which compares the confining pressure to the characteristic pressure $P_\star$ controlling the lubrication transition, and the dimensionless coating thickness $\tilde{b}$. Secondly, this approach clarifies the role of the physical parameters in our system. The viscosity η, the particle diameter d, and the critical lubrication number at the transition $\mathcal{L}_\star^\infty$ are encoded in $P_\star$. The other parameters of the tribology law, namely, the dry and lubricated friction coefficients μ_{dry} and μ_{lub}^∞, as well as the width of the lubrication transition $\Delta\mathcal{L}$ (which may depend on the particle diameter), come into play in the expression for μ_p. In the model, we set $\mu_{dry} = 0.5$ and $\mu_{lub}^\infty = 0.05$, values higher than the experimental measurements ($\mu_{dry} = 0.1$ and $\mu_{lub}^\infty = 0.02$). These adjusted parameters provide a better agreement between the predictions of the mean-field model and the experimentally observed bulk friction, and are later used consistently in the DEM simulations (see below).

In Fig. 5(a) and (b), we summarize the prediction of the model for the two constitutive laws, $\mu(I)$ and $\phi(I)$, for different dimensionless pressures $P/P_\star$, while $\tilde{b}$ and $\Delta\mathcal{L}$ are kept fixed. For large pressures $P \gg P_\star$, the friction law and volume fraction are independent of P and correspond to the non-lubricated dry case for the range of inertial number investigated. In this regime $\bar{\mathcal{L}}/\mathcal{L}_\star^\infty$ remains small. Conversely, for low pressures $P \ll P_\star$, the rheology is also pressure-independent but corresponds to the fully lubricated case where $\bar{\mathcal{L}}/\mathcal{L}_\star^\infty \gg 1$. For intermediate pressures, the rheological curves transition between these two extremes through a velocity-weakening branch, where the friction decreases with increasing I. This scenario remains qualitatively unchanged when varying the coating thickness $\tilde{b} > 1$. Decreasing $\tilde{b}$ simply shifts the low friction limit towards higher friction coefficients and lower volume fractions, as shown in Fig. 5(c) and (d). This picture also depends on the sharpness of the lubrication transition at the contact. The effect of $\Delta\mathcal{L}$ is shown in Fig. 5(e) and (f), where $\mu(I)$ and $\phi(I)$ relationships are plotted for different values of $\Delta\mathcal{L}$, while $P/P_\star = 10^{-5}$ and $\tilde{b} = 5$ are kept fixed. The non-monotonic behaviour is amplified when $\Delta\mathcal{L}$ is small, whilst it is mitigated when $\Delta\mathcal{L}$ increases, meaning that the transition is smooth enough that the system displays a roughly constant friction coefficient for these values of I (yellow curve).

The predictions of this simple mean-field approach can be compared with the experimental observations previously presented in Fig. 2. While a quantitative comparison is not feasible, since the lubrication transition at the particle scale

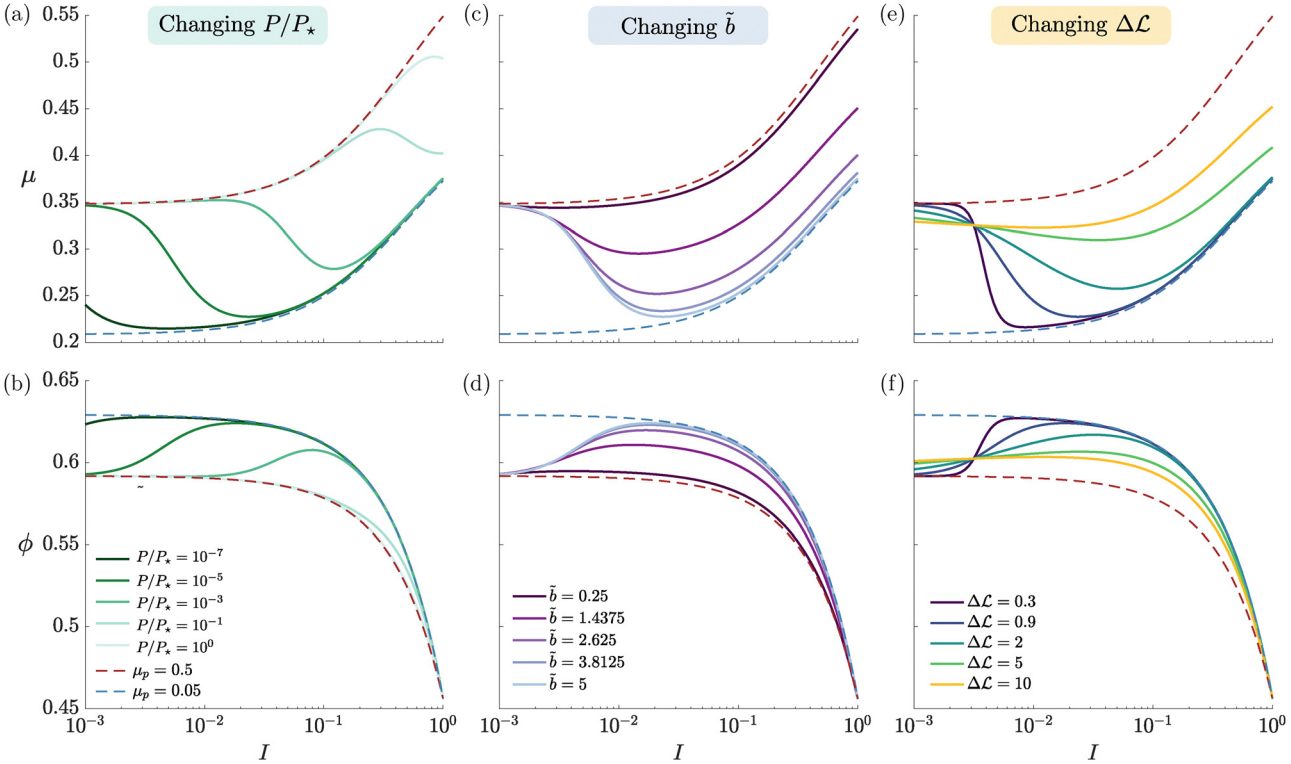

Fig. 5 Constitutive laws computed with the mean field model. (a) $\mu(I)$ and (b) $\phi(I)$ for $\tilde{b}$ = 5, $\Delta\mathcal{L} = 0.9$, and different values of $P/P_\star$. In panels (c) and (d) the constitutive laws are plotted also for d = 3.0 mm, $P/P_\star = 10^{-5}$, and $\Delta\mathcal{L} = 0.9$, while the non-dimensional coating thickness $\tilde{b}$ is varied. The effect of $\Delta\mathcal{L}$ is investigated in (e) and (f), where it is shown the constitutive laws fixed $P/P_\star = 10^{-5}$, $\tilde{b}$ = 5, and different values of $\Delta\mathcal{L}$. In all panels, the particle size d = 3 mm is kept fixed, solid lines represent results for the mean field model, whereas dashed lines depict the results for constant interparticle friction μ_p = 0.5 (red) and μ_p = 0.05 (blue).

occurs at much higher coating thicknesses b than the transition observed in bulk rheology, the mean-field approach successfully captures several key experimental trends. It recalls the effect of the coating thickness, *i.e.* larger thicknesses lead to lower bulk friction coefficient and denser packings. It also reproduces the role of confining pressure, which governs the transition from low-frictional to high-frictional behavior, as well as the influence of the inertial number, which plays an opposing role in this transition. Additionally, depending on the chosen parameters, the model predicts the emergence of a shear-weakening branch consistent with experimental observations.

To further explore the link between tribology and bulk rheology, we extend our analysis in the next section by performing Discrete Element Method (DEM) simulations. These simulations incorporate a non-constant interparticle friction coefficient to explicitly reproduce the lubrication transition. This approach allows us to assess the limitations of the mean-field model, whose assumptions may be too drastic.

7 Lubrication in discrete element simulations

To further investigate the link between the lubrication transition at the particle scale and the frictional transition in the bulk rheology of polymer-coated particles, we perform Discrete Element Method (DEM) simulations using the open-source software LAMMPS.[44] In these simulations, the granular material consists of frictional spherical particles with a diameter d and an intrinsic density ρ_g = 2500 kg m^{-3}. The particles interact *via* a Hertz-Mindlin contact model,[45] with a Poisson ratio ν = 0.3, Young modulus $E = 10^7$ Pa, and a restitution coefficient e = 0.2.

Simulations are conducted in a plane shear configuration, where the top and bottom rigid plates are made rough by fixing particles identical to those in the bulk. The simulation box has dimensions $(L_x, L_y) = (20d, 20d)$ with a typical thickness $h = 6d$ at rest, thin enough to prevent localisation as in the experiments. Periodic boundary conditions are applied in the flow (x) and lateral (y) directions. The bottom plate remains fixed, while a horizontal velocity $U\mathbf{e}_x$ is imposed on the top plate, where $\mathbf{e}_x$ is the unit vector in the x direction. To simulate the pressure-imposed configuration, the upper plate is subjected to a constant pressure P but is free to move vertically, allowing the material to dilate or compact by adjusting the flow thickness, h. Each simulation follows the experimental protocol: for a given imposed pressure, different constant velocities are applied to the top plate to sweep a range of inertial numbers $I = \dot{\gamma} d \Big/ \sqrt{P/\rho_g}$ under constant pressure conditions. Once the system reaches a steady state, the shear stress τ and volume

fraction ϕ are measured to obtain the friction coefficient μ and the volume fraction ϕ. In the steady state, we verify that for all configurations, the velocity profile is linear, implying that $\dot{\gamma} = U/h$, and the volume fraction is uniform across the granular layer.

The non-Coulombic frictional behavior of the polymer-coated particles is modelled *via* a non-constant interparticle friction coefficient μ_p, defined by (8). As in the mean-field model, we use $\mu_{dry} = 0.5$ and $\mu_{lub}^{\infty} = 0.05$, slightly higher than the experimental values, so that the resulting bulk friction coefficient μ_c and solid fraction ϕ_c reproduce the experimental observations. At each timestep, the relative sliding velocity V^i and normal force F_n^i are computed for all existing contacts i. This sets the lubrication number $\mathcal{L}^i$ at each contact, given by the following relationship when writing (5) using the characteristic pressure P (eqn (10)):

$$\frac{\mathcal{L}^i}{\mathcal{L}_\star^\infty} = \frac{V^i d^2}{F_n^i}\sqrt{\rho_g P_\star}. \tag{13}$$

Eqn (8) then provides the local interparticle friction coefficient at contact i: $\mu_p\left(\mathcal{L}^i/\mathcal{L}_\star^\infty\right)$.

The results of the simulations are shown in Fig. 6 for different pressures $P/P^\star$, coating thicknesses $\tilde{b}$, and widths of the lubrication transition $\Delta\mathcal{L}$. The square markers correspond to the constitutive laws with a constant μ_p, equal to the high-frictional limit $\mu_p = 0.5$ for the blue squares and the low-frictional limit $\mu_p = 0.05$ for the red squares.

We find that the DEM simulations capture the key qualitative features observed experimentally and predicted by the mean-field model. First, decreasing the pressure or increasing the coating thickness induces a decrease in the friction coefficient and an increase in the volume fraction, which is the signature of the lubrication transition. The DEM simulations also show that increasing the inertial number enhances the lubrication effect in the rheology, leading to a non-monotonic friction law and the appearance of a shear-weakening branch.

A closer comparison of the mean-field model and the DEM, both constructed on the same microscopic basis, reveals an important difference: the DEM predicts a much smoother transition with I than the mean-field approach for the same parameter values ($P/P_\star$, $\tilde{b}$, $\Delta\mathcal{L}$). For the smallest values of $\Delta\mathcal{L}$, corresponding to an abrupt interparticle lubrication transition, the mean-field model shows an abrupt transition in the bulk rheology, whereas the DEM exhibits a smooth transition. This discrepancy can be explained by the existence in the DEM of a wide distribution of sliding velocities and normal forces across contacts, while the mean-field model only considers averaged values. The width of the transition is thus controlled by the entire distribution of $\mathcal{L}^i$ among the contacts rather than by $\Delta\mathcal{L}$ alone. In Appendix A, we present a modification of the mean-field theory that accounts for the full distribution of $\mathcal{L}^i$

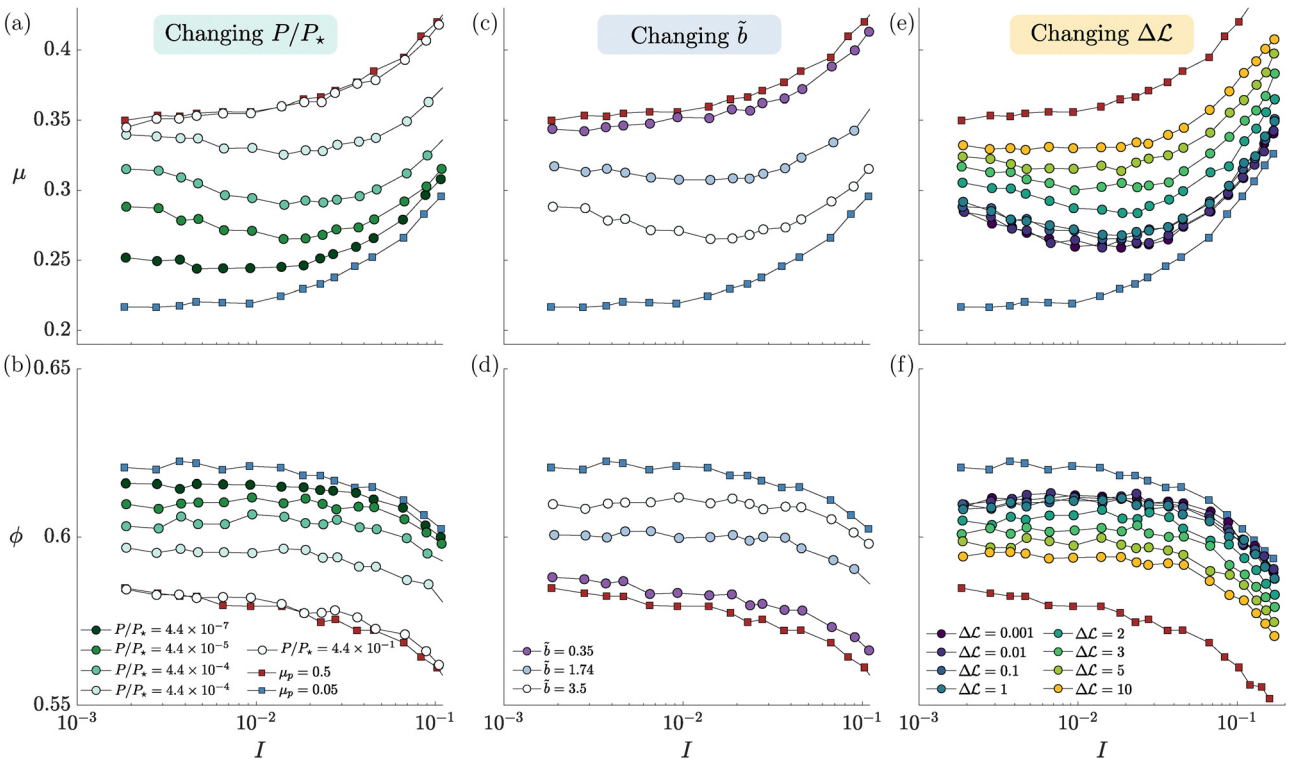

Fig. 6 Constitutive laws measured with DEM simulations. (a) $\mu(I)$ and (b) $\phi(I)$ for $\tilde{b} = 3.5$, $\Delta\mathcal{L} = 0.9$, and different dimensionless pressures $P/P_\star$. In (c) and (d) the rheology is plotted for fixed $P/P_\star = 10^{-5}$ and $\Delta\mathcal{L} = 0.9$, while $\tilde{b}$ is varied. In (e) and (f), $P/P_\star = 10^{-5}$ and $\tilde{b} = 3.5$ are kept constant, whilst the effect of $\Delta\mathcal{L}$ is investigated. In all panels, $d = 1$ mm is kept fixed and circles represent the results for the coated granular material, whereas squares depict the results for constant interparticle friction $\mu_p = 0.5$ (red) and $\mu_p = 0.05$ (blue).

measured in the DEM to compute an effective interparticle friction coefficient $\bar{\mu}_p$, which improves the agreement between the model and the DEM simulations.

8 Conclusions

This study investigates the rheology of polymer-coated granular materials through a combined approach of laboratory experiments, a mean-field model, and Discrete Element Method (DEM) simulations. We demonstrate that the presence of a thin polymer coating drastically affects the rheology of the granular media, enabling access to a low-frictional, lubricated state. In this state, the bulk friction decreases and the material becomes denser compared to the dry, uncoated case. The constitutive laws, $\mu(I)$ and $\phi(I)$, explicitly depend on the imposed normal stress and the shear rate. The rheology converges towards the frictional state as pressure increases, while increasing the shear rate $\dot{\gamma}$ shifts the system toward the low frictional regime, revealing non-monotonic behavior in the friction law.

This complex rheological behavior originates from a lubrication transition occurring at the particle scale. Using a four-ball tribometer, we measured the interparticle friction coefficient μ_p to show that the coating induces a non-Coulombic frictional response between individual grains. The friction coefficient μ_p varies with both the normal force and sliding velocity between the particles, transitioning from near-zero values (for sufficiently thick coatings) to the dry case under higher pressure or slower sliding. By systematically varying particle size, coating thickness, normal force, and sliding velocity, we introduce a dimensionless lubrication number $\mathcal{L}$, which collapses the experimental tribology data. At low $\mathcal{L}$ values, the friction coefficient matches that of uncoated glass beads, while at high $\mathcal{L}$, it decreases towards a lower value dependent on the coating thickness b.

Incorporating the experimentally measured interparticle friction law into DEM simulations qualitatively captures all the key features observed in the macroscopic rheology, confirming that the complex bulk behavior originates from the frictional transition at the particle scale. We also derived a theoretical mean-field model, assuming that the rheology of coated particles can be described by constitutive equations for dry, uncoated particles if the non-Coulombic interparticle behavior is incorporated into an effective friction coefficient.

While we can qualitatively describe the lubrication transition, a precise quantitative comparison between experiments, DEM, and the mean-field model remains challenging. In bulk rheology, lubrication effects are already observed for coating thicknesses below $\sim$100 nm, whereas particle-scale tribology measurements indicate that significant interparticle lubrication only occurs for coatings thicker than $\sim$200 nm. The origin of this mismatch is not fully understood, but it may involve heterogeneities in the coating or collective effects in the granular assembly that amplify lubrication at smaller thicknesses.

This difficulty illustrates the broader challenge of linking microscopic interactions to macroscopic flow in granular materials. Even for dry systems, achieving quantitative agreement typically requires using microscopic friction coefficients in DEM simulations that are larger than those measured experimentally. The same principle applies here: when lubrication is introduced, multiscale effects persist, and microscopic parameters must be adjusted to capture the observed macroscopic behavior.

Although this study does not provide a complete picture of polymer-coated granular rheology, our findings have direct implications for addressing flowability challenges in industrial settings. Just as the use of superplasticizers in concrete has evolved from empirical practice to a rationalized framework based on frictional transition models,[46,47] our results pave the way for a deeper understanding of how polymers and lubricants can manipulate and control the flow properties of dry granular materials and powders. Notably, the non-monotonic behavior induced by the coating may critically influence macroscopic dynamics, potentially generating flow instabilities and the coexistence of static and flowing states,[35,48–51] phenomena of significant relevance in industrial applications.

Author contributions

FMR contributed to performing and analysing rheology and tribology experiments, developing the mean-field model, and writing the original version of the manuscript. DD developed the numerical code, performed all the DEM simulations, and contributed to the development of the mean-field model. FT and AG contributed to performing and analysing the rheological experiments. VB contributed to the development of the mean-field model. MN and OP contributed to the conceptualization and to the analysis of all experimental, numerical and theoretical results. All authors contributed to revising and editing the manuscript.

Conflicts of interest

There are no conflicts to declare.

Data availability

Once the paper is accepted, the datasets generated during the current study will be available at the repository Zenodo (https://doi.org/10.5281/zenodo.18199465).

Appendix

A. Modified mean field model

To account for the distribution of contact lubrication number $\mathcal{L}^i$ measured in the DEM, here we present a modified mean field model. The main extension of the model consists in considering that, even when the pressure P and shear rate $\dot{\gamma}$ are prescribed, and the system achieves a steady state, the contact sliding velocity V and normal force F_n are not

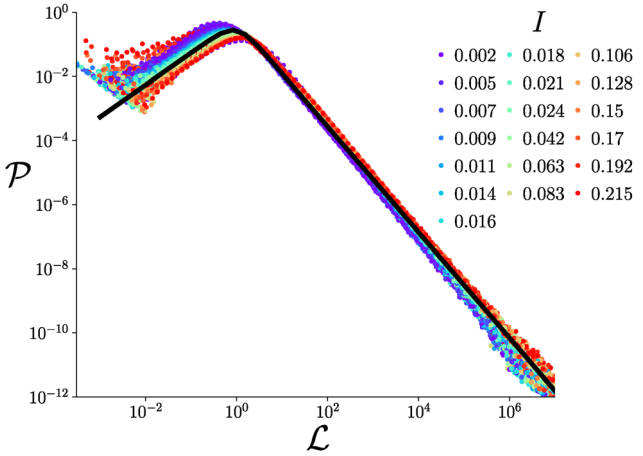

Fig. 7 Probability distribution function of lubrication numbers $\mathcal{L}$ within the material for different inertial numbers I. Results are obtained from DEM simulations, where $\mathcal{P}$ was reconstructed from the distribution of contact sliding velocity and normal forces for a granular material with Coulombic constant interparticle friction μ_p = 0.5.

homogeneously distributed within the material. Instead, there is a distribution of V/F_n across established contacts, which depends on the inertial number I. In this case, we assume that the constitutive laws $\mu(I, \bar{\mu}_p(I, \tilde{b}))$ and $\phi(I, \bar{\mu}_p(I, \tilde{b}))$ become functions of the average interparticle friction coefficient $\bar{\mu}_p(I, \tilde{b})$, which incorporates the heterogeneities in $\mathcal{L}$ throughout the medium.

The average interparticle friction is then defined as

$$\bar{\mu}_p(I, \tilde{b}) = \int_0^\infty \mu_p\left(\mathcal{L}/\mathcal{L}_\star^\infty, \tilde{b}\right)\mathcal{P}(\mathcal{L}, I)\mathrm{d}\mathcal{L}, \quad \text{(S1)}$$

where $\mu_p\left(\mathcal{L}/\mathcal{L}_\star^\infty, \tilde{b}\right)$ is the interparticle friction law measured experimentally and expressed by (8), while $\mathcal{P}(\mathcal{L}/\mathcal{L}_\star^\infty, I)$ is the probability distribution of $\mathcal{L}$ throughout the material. Here, we assume that the probability distribution of V/F_n for the coated particles takes the same form as in an ensemble of uncoated grains. This assumption is the same as the one used in Dumont *et al.* (2025), however, in their case the interparticle friction was only a function of the normal force F_n. The functional form of $\mathcal{P}(\mathcal{L}/\mathcal{L}_\star^\infty, I)$ is computed by first performing DEM simulations for grains with constant Coulombic friction μ_p = 0.5 to obtain the probability distribution of V/F_n within the material for different inertial numbers (Fig. 7). For a given set of particles and polymer properties, d, $\tilde{b}$ and η, and since $\mathcal{P}$ depends only weakly on the value of μ_p,[25] the distribution of $\mathcal{L}$ throughout established contacts is well rationalized by the following expression:

$$\mathcal{P}(\mathcal{L}, I) = \frac{\alpha}{\mathcal{L}_{\max}(I)}\frac{\mathcal{L}/\mathcal{L}_{\max}(I)}{1 + [\mathcal{L}/\mathcal{L}_{\max}(I)]^\beta}, \quad \text{(S2)}$$

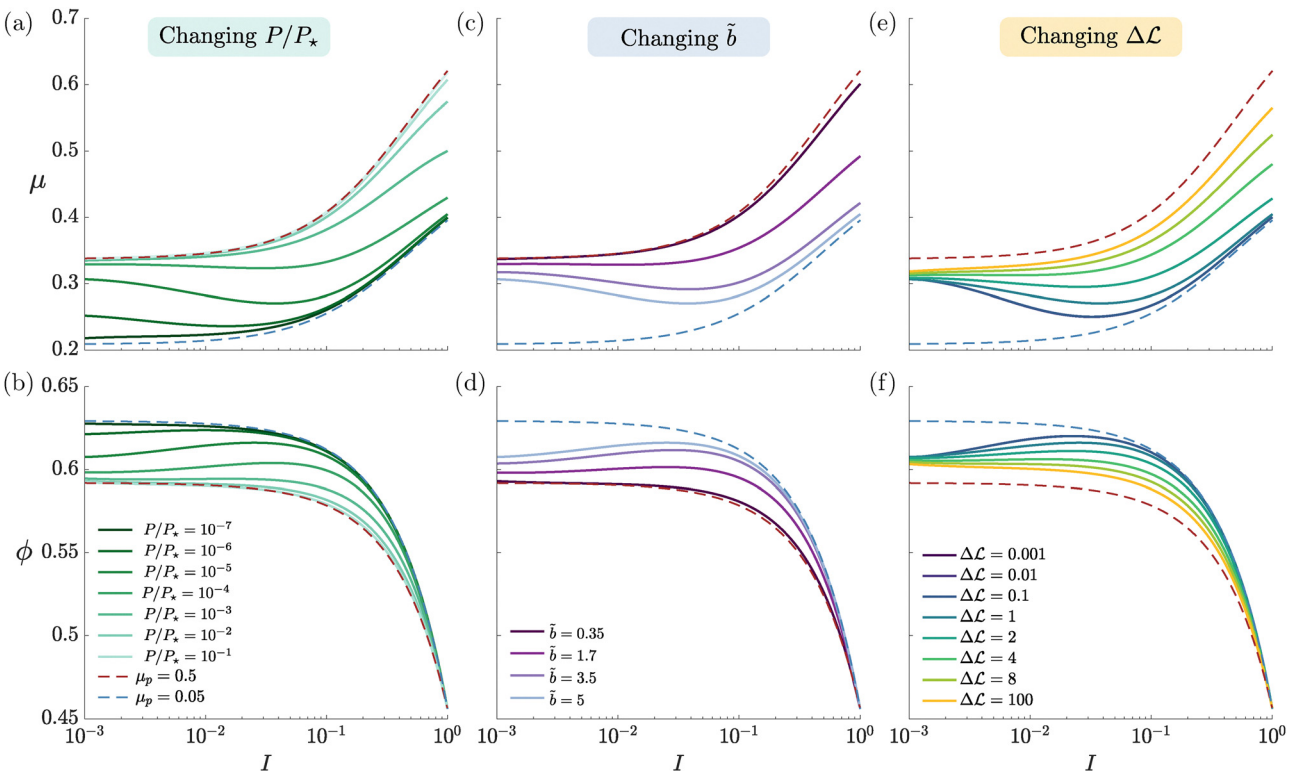

Fig. 8 Constitutive laws computed with the extended mean field model. (a) $\mu(I)$ and (b) $\phi(I)$ for $\tilde{b}$ = 5, $\Delta\mathcal{L} = 0.9$, and different values of $P/P_\star$. In panels (c) and (d) the flow rules are plotted also for d = 3.0 mm, $P/P_\star = 10^{-5}$, $\Delta\mathcal{L} = 0.9$, while the non-dimensional coating thickness $\tilde{b}$ is varied. The effect of $\Delta\mathcal{L}$ is investigated in (e) and (f), where it is shown the flow rules fixed $P/P_\star = 10^{-5}$, $\tilde{b}$ = 5, and different values of $\Delta\mathcal{L}$. In all panels, the particle size d = 3 mm is kept fixed, solid lines represent results for the mean field model, whereas dashed lines depict the results for constant interparticle friction μ_p = 0.5 (red) and μ_p = 0.05 (blue).

where $\alpha = 0.55$ and $\beta = 2.65$ are fitting parameters, while

$$\mathcal{L}_{\max}(I) = \mathcal{L}_\star^\infty \sqrt{\frac{P_\star}{P}} \mathcal{F}(I), \tag{S3}$$

represents the position where the distribution reaches its maximum value. We observe that the data for all value of I can be collapsed by fitting $\mathcal{F}(I) = 0.042\sqrt{I}$.

Substituting the expression for the probability distribution (S2) and the experimentally measured interparticle friction law (8) into the definition of $\tilde{\mu}_p$ (S1), and solving the integral, one obtains the average interparticle friction coefficient as a function of the inertial number and the non-dimensional coating thickness $\tilde{b}$. Once $\tilde{\mu}_p$ is computed for all values of I, one can compute the parameters $\mu_c(\tilde{\mu}_p)$, $\mu_\infty(\tilde{\mu}_p)$, $\phi_c(\tilde{\mu}_p)$, and $\phi_m(\tilde{\mu}_p)$ (see for instance Appendix of Dumont *et al.* (2025)[25]) to obtain the constitutive flow rules $\mu(I)$ and $\phi(I)$.

The results of the extended mean-field model are plotted in Fig. 8(a)–(f). Taking into account the distribution of $\mathcal{L}$ within the material does not change the overall picture of the effect of the non-Coulombic interparticle friction on the material's rheology. The same qualitative behaviours are observed when the non-dimensional pressure, coating thickness, and width of the distribution are varied. However, taking into account the heterogeneities in contact normal force and sliding velocity smooths the transition between the two frictional states. Accounting for the distribution of $\mathcal{L}^i$ improves the agreement between the mean-field model and results from DEM simulations, however quantitative discrepancies still remain.

The quantitative discrepancies observed here contrast with the findings of Dumont *et al.* (2025),[25] where quantitative agreement was reported between a mean-field approach and DEM for grains with a normal-force-dependent friction coefficient. We hypothesize that the velocity dependence introduced in the current study creates additional correlations between tangential motion and the friction coefficient, which are not captured by the mean-field model.

Acknowledgements

This project has received funding from the European Research Council (ERC) under the European Union's Horizon (Grant No. 101097842). The authors also acknowledge financial support from International Fine Particle Research Institute (IFPRI) and the Agence Nationale de la Recherche under RheoCom Grant No. ANR-22-CE06-0020.

References

1 B. Andreotti, Y. Forterre and O. Pouliquen, *Granular media: between fluid and solid*, Cambridge University Press, 2013.
2 T. Shinbrot and F. J. Muzzio, *Phys. Rev. Lett.*, 1998, **81**, 4365–4368.
3 J. M. N. T. Gray, *Ann. Rev. Fluid Mech.*, 2018, **50**, 407–433.
4 A. A. Tracton, *Coatings technology handbook*, CRC Press, 2005.
5 GDR-MiDi, *Eur. Phys. J. E: Soft Matter Biol. Phys.*, 2004, **14**, 341–365.
6 F. Da Cruz, S. Emam, M. Prochnow, J.-N. Roux and F. Chevoir, *Phys. Rev. E: Stat., Nonlinear, Soft Matter Phys.*, 2005, **72**, 021309.
7 P. Jop, Y. Forterre and O. Pouliquen, *Nature*, 2006, **44**, 727–730.
8 M. Bouzid, M. Trulsson, P. Claudin, E. Clément and B. Andreotti, *Phys. Rev. Lett.*, 2013, **111**, 238301.
9 K. Kamrin and D. L. Henann, *Soft Matter*, 2015, **11**, 179–185.
10 A. N. Edwards, A. S. Russell, C. G. Johnson and J. M. N. T. Gray, *J. Fluid Mech.*, 2019, **875**, 1058–1095.
11 T. Barker, M. Rauter, E. S. F. Maguire, C. G. Johnson and J. M. N. T. Gray, *J. Fluid Mech.*, 2021, **909**, A22.
12 R. S. Sharma and A. Sauret, *Soft Matter*, 2025, **21**, 2193–2208.
13 O. Pouliquen, *Rheol. Acta*, 2025, 1–13.
14 S. Chialvo, J. Sun and S. Sundaresan, *Phys. Rev. E: Stat., Nonlinear, Soft Matter Phys.*, 2012, **85**, 021305.
15 G. Grosjean and S. Waitukaitis, *Phys. Rev. Lett.*, 2023, **130**, 098202.
16 C.-P. Hsu, S. N. Ramakrishna, M. Zanini, N. D. Spencer and L. Isa, *Proc. Natl. Acad. Sci. U. S. A.*, 2018, **115**, 5117–5122.
17 C.-P. Hsu, J. Mandal, S. N. Ramakrishna, N. D. Spencer and L. Isa, *Nat. Commun.*, 2021, **12**, 1477.
18 N. M. James, E. Han, R. A. L. de la Cruz, J. Jureller and H. M. Jaeger, *Nat. Mater.*, 2018, **17**, 965–970.
19 N. M. James, C.-P. Hsu, N. D. Spencer, H. M. Jaeger and L. Isa, *J. Phys. Chem. Lett.*, 2019, **10**, 1663–1668.
20 Y. Moratille, M. Arshad, C. Cohen, A. Maali, E. Lemaire, N. Sintes-Zydowicz and E. Drockenmuller, *J. Colloid Interface Sci.*, 2022, **607**, 1687–1698.
21 C. Clavaud, A. Bérut, B. Metzger and Y. Forterre, *Proc. Natl. Acad. Sci. U. S. A.*, 2017, **114**, 5147–5152.
22 H. Perrin, C. Clavaud, M. Wyart, B. Metzger and Y. Forterre, *Phys. Rev. X*, 2019, **9**, 031027.
23 J.-C. Tsai, G.-H. Huang and C.-E. Tsai, *Phys. Rev. Lett.*, 2021, **126**, 128001.
24 C.-E. Tsai, W.-C. Li, H.-C. Fan-Chiang, P.-Y. Hsiao and J.-C. Tsai, *Phys. Rev. Res.*, 2024, **6**, 023065.
25 D. Dumont, F. M. Rocha, M. Nicolas and O. Pouliquen, *Phys. Rev. Fluids*, 2025, **10**, 064302.
26 A. Gans, O. Pouliquen and M. Nicolas, *Phys. Rev. E*, 2020, **101**, 032904.
27 A. Gans, A. Abramian, P.-Y. Lagrée, M. Gong, A. Sauret, O. Pouliquen and M. Nicolas, *J. Fluid Mech.*, 2023, **959**, A41.
28 R. S. Sharma, W. Sarlin, L. Xing, C. Morize, P. Gondret and A. Sauret, *Phys. Rev. Fluids*, 2024, **9**, 074301.
29 A. Gans, B. Dalloz-Dubrujeaud, M. Nicolas and P. Aussillous, *Phys. Rev. Lett.*, 2024, **133**, 238201.
30 A. Pol, R. Artoni and P. Richard, *J. Fluid Mech.*, 2025, **1006**, A24.
31 P.-E. Peyneau and J.-N. Roux, *Phys. Rev. E: Stat., Nonlinear, Soft Matter Phys.*, 2008, **78**, 011307.
32 N. Estrada, A. Taboada and F. Radjai, *Phys. Rev. E: Stat., Nonlinear, Soft Matter Phys.*, 2008, **78**, 021301.
33 F. Tapia, O. Pouliquen and É. Guazzelli, *Phys. Rev. Fluids*, 2019, **4**, 104302.

34 T. Man, P. Zhang, Z. Ge, S. A. Galindo-Torres and K. M. Hill, *Acta Mech. Sin.*, 2023, **39**, 722191.
35 T. Divoux, M. A. Fardin, S. Manneville and S. Lerouge, *Annu. Rev. Fluid Mech.*, 2016, **48**, 81–103.
36 S. Mandal, M. Nicolas and O. Pouliquen, *Phys. Rev. X*, 2021, **11**, 021017.
37 M. Workamp and J. A. Dijksman, *J. Rheol.*, 2019, **63**, 275–283.
38 J. L. Anthony and C. Marone, *J. Geophys. Res.: Solid Earth*, 2005, **110**, B8.
39 J. Bongaerts, K. Fourtouni and J. Stokes, *Tribol. Int.*, 2007, **40**, 1531–1542.
40 B. Veltkamp, K. Velikov, C. Venner and D. Bonn, *Phys. Rev. Lett.*, 2021, **126**, 044301.
41 H. Dong, N. Moyle, H. Wu, C. Y. Khripin, C.-Y. Hui and A. Jagota, *Adv. Mater.*, 2023, **35**, 2211044.
42 B. Persson and M. Scaraggi, *J. Phys.: Condens. Matter*, 2009, **21**, 185002.
43 L. Lobry, E. Lemaire, F. Blanc, S. Gallier and F. Peters, *J. Fluid Mech.*, 2019, **860**, 682–710.
44 A. P. Thompson, H. M. Aktulga, R. Berger, D. S. Bolintineanu, W. M. Brown, P. S. Crozier, P. J. In't Veld, A. Kohlmeyer, S. G. Moore and T. D. Nguyen, *et al.*, *Comput. Phys. Commun.*, 2022, **271**, 108171.
45 R. D. Mindlin and H. Deresiewicz, *J. Appl. Mech.*, 1953, **16**, 327–330.
46 G. Bossis, Y. Grasselli and O. Volkova, *Rheol. Acta*, 2022, **61**, 1–12.
47 J. A. Richards, R. E. O'Neill and W. C. K. Poon, *Rheol. Acta*, 2021, **60**, 97–106.
48 A. Daerr and S. Douady, *Nature*, 1999, **399**, 241–243.
49 O. Pouliquen and Y. Forterre, *J. Fluid Mech.*, 2002, **453**, 133–151.
50 J. A. Dijksman, G. H. Wortel, L. T. Van Dellen, O. Dauchot and M. Van Hecke, *Phys. Rev. Lett.*, 2011, **107**, 108303.
51 C. Ness and S. M. Fielding, *Phys. Rev. Lett.*, 2025, **134**, 038201.